

1 High-order dynamic neural correlations reflect naturalistic 2 processing in humans

Lucy L. W. Owen¹, Thomas H. Chang^{1,2}, and Jeremy R. Manning^{1,†}

¹Department of Psychological and Brain Sciences,
Dartmouth College, Hanover, NH

³Amazon.com, Seattle, WA

[†]Address correspondence to jeremy.r.manning@dartmouth.edu

August 1, 2019

Abstract

Our thoughts arise from coordinated activity patterns across our brain. We examined high-order dynamic correlations in functional neuroimaging data collected as human participants listened to different auditory stimuli varying in cognitive richness, along with an additional resting state condition. Our approach combines a kernel-based method for estimating the dynamic functional correlations that are similar (within task) across participants, along with a dimensionality reduction approach that enables us to efficiently compute high-order correlations in the data. We trained classifiers to decode the precise time, relative to the start of the stimulus, when a given neural pattern was recorded. We trained these classifiers using the neural activity timeseries, first-order dynamic correlations, and higher-order correlations (up to tenth-order correlations), and asked which types of features led to the highest decoding accuracy. We found that higher-order correlations consistently yielded higher decoding accuracy for the most cognitively rich condition of the experiment, whereas first-order correlations or raw data yielded the highest decoding accuracy at for the less cognitively rich conditions as well as rest.

18 Introduction

19 To understand the neuronal computations that support cognition, we must understand the cooperative
20 dynamics of populations of neurons. These populations of neurons interact within each brain structure,
21 and the structures interact to form complex and dynamic networks. These interactions, at each scale, vary
22 according to the functions our brains are carrying out and recent work has shown these dynamic complex
23 patterns support consciousness (Demertzi et al., 2019).

In the last several decades, advances in functional magnetic resonance image (fMRI) analyses have evolved to better characterize these interactions of brain structures. As Turk-Browne (2013) outlines, analyses using multivariate patterns of activity have given an advance over univariate activity patterns because they allow relative contributions of voxels to be combined and better assess distributed representations. Resting-state connectivity (RS) fMRI, which is the temporal correlation of regions during rest, has shed light on the rich and complex spatiotemporal organization of spontaneous brain activity. Functional connectivity

30 (FC) has further characterized the cognitive state dependency of this network organization.

31 Recent work has shown that FC fluctuates over time (Chang & Glover, 2010) (? for review), and
32 the assumed stationarity of these analyses may be too simple to capture the dynamic nature of brain
33 activity. Additionally, recent work has shown that temporal variability in functional connectivity predicts
34 attention task performance (?) and that dynamic correlations between multivariate voxel patterns can add
35 an additional boost compared to static multivariate voxel patterns alone (Manning et al., 2018).

36 Following this line of reasoning, we expect higher-order network dynamics might provide even richer
37 insights into the neural basis of cognition. We sought to test this hypothesis by developing an approach
38 to inferring high-order network dynamics from timeseries data, validating the approach using synthetic
39 data, and then applying the approach to a neuroimaging dataset comprising data collected as participants
40 listened to a story varying in cognitive richness (Simony et al., 2016).

41 Methods

42 A major challenge to studying such patterns is that typically neither the correlations nor the hierarchical
43 organizations of those correlations may be directly observed. Rather, these fundamental properties must
44 be inferred indirectly by examining the observable parts of the system—e.g., the behaviors of the individual
45 units of that system. Here we propose a series of mathematical operations that may be used to approximate
46 dynamic correlations at a range of scales (i.e., orders of interaction).

47 There are two basic steps to our approach (Fig. 2). In the first step, we take a number-of-timepoints (T)
48 by number-of-features (F) *matrix of observations* (\mathbf{X}) and we return a T by $\frac{F^2-F}{2}$ *matrix of dynamic correlations*
49 (\mathbf{Y}_0). Here \mathbf{Y}_0 describes, at each moment, how all of the features (columns of \mathbf{X}) are inferred to be interacting.
50 (Since the interactions are assumed to be non-recurrent and symmetric, only the upper triangle of the full
51 correlation matrix is computed.) In the second step, we project \mathbf{Y}_0 onto an F -dimensional space, resulting in
52 a new T by F matrix \mathbf{Y}_1 . Note that \mathbf{Y}_1 contains information about the correlation dynamics present in \mathbf{X} , but
53 represented in a compressed number of dimensions. By repeatedly applying these two steps in sequence,
54 we can examine and explore higher order dynamic correlations in \mathbf{X} .

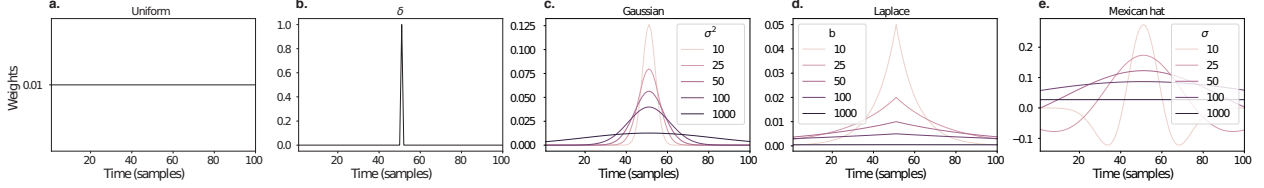


Figure 1: **Examples of time-varying weights.** Each panel displays per-timepoint weights at $t = 50$, evaluated for 100 timepoints (1, ..., 100). **a. Uniform weights.** The weights are timepoint-invariant; observations at all timepoints are weighted equally, and do not change as a function of t . This is a special case of weight function that reduces dynamic correlations to static correlations. **b. Dirac delta function.** Only the observation at timepoint t is given weight (of 1), and weights for observations at all other timepoints are set to 0. **c. Gaussian weights.** Each observation's weights fall off in time according to a Gaussian probability density function centered on $\mu = t$. Weights derived using several different example variance parameters (σ^2) are displayed. **d. Laplace weights.** Each observation's weights fall off in time according to a Laplace probability density function centered on $\mu = t$. Weights derived using several different example scale parameters (b) are displayed. **e. Mexican hat (Ricker wavelet) weights.** Each observation's weights fall off in time according to a Ricker wavelet centered on t . This function highlights the *contrasts* between local versus surrounding activity patterns in estimating dynamic correlations. Weights derived using several different example width parameters (σ) are displayed.

55 Dynamic correlations

Given a matrix of observations, we can compute the (static) correlations between any pair of observations, \mathbf{X}_i and \mathbf{X}_j using:

$$\text{corr}(\mathbf{X}_i, \mathbf{X}_j) = \frac{\sum_{t=1}^T (\mathbf{X}_i(t) - \bar{\mathbf{X}}_i)(\mathbf{X}_j(t) - \bar{\mathbf{X}}_j)}{\sqrt{\sum_{t=1}^T \sigma_{\mathbf{X}_i}^2 \sigma_{\mathbf{X}_j}^2}}, \text{ where} \quad (1)$$

$$\bar{\mathbf{X}}_k = \sum_{t=1}^T \mathbf{X}_k(t), \text{ and} \quad (2)$$

$$\sigma_{\mathbf{X}_k}^2 = \sum_{t=1}^T (\mathbf{X}_k(t) - \bar{\mathbf{X}}_k)^2 \quad (3)$$

56 We can generalize this formula to compute time-varying correlations by incorporating a *weight function*
 57 that takes a time t as input, and returns how much the observed data every timepoint (including t) contribute
 58 to the correlations at time t (Fig. 1).

Given a weight function $w(t)$ for timepoint t , evaluated at timepoints in the interval $[1, \dots, T]$, we can

extend the static correlation formula in Equation 2 to reflect an *instantaneous correlation* at timepoint t :

$$\text{timecorr}(\mathbf{X}_i, \mathbf{X}_j, t) = \frac{\sum_{t=1}^T (\mathbf{X}_i(t) - \tilde{\mathbf{X}}_i(t))(\mathbf{X}_j(t) - \tilde{\mathbf{X}}_j(t))}{\sqrt{\sum_{t=1}^T \tilde{\sigma}_{\mathbf{X}_i}^2(t) \tilde{\sigma}_{\mathbf{X}_j}^2(t)}}, \text{ where} \quad (4)$$

$$\tilde{\mathbf{X}}_k(t) = \sum_{i=1}^T w(t, i) \mathbf{X}_k(i), \quad (5)$$

$$\tilde{\sigma}_{\mathbf{X}_k}^2(t) = \sum_{i=1}^T (\mathbf{X}_k(i) - \tilde{\mathbf{X}}_k(t))^2, \quad (6)$$

and $w(t, i)$ is shorthand for $w(t)$ evaluated at timepoint i . Equation 5 may be used to estimate the instantaneous correlations between every pair of observations, at each timepoint (i.e., \mathbf{Y}).

61 Inter-subject dynamic correlations

Equation 5 provides a means of taking a single observation matrix, \mathbf{X} and estimating the dynamic correlations from moment to moment, \mathbf{Y} . Suppose that one has access to a set of multiple observation matrices that reflect the same phenomenon. For example, one might collect neuroimaging data from several experimental participants, as each participant performs the same task (or sequence of tasks). Let $\mathbf{X}_1, \mathbf{X}_2, \dots, \mathbf{X}_P$ reflect the T by F observation matrices for each of P participants in an experiment. We can use *inter-subject functional connectivity* (ISFC; Simony et al., 2016) to compute the degree of stimulus-driven correlations reflected in the multi-participant dataset at a given timepoint t using:

$$\bar{\mathbf{C}}(t) = M \left(R \left(\frac{1}{2P} \sum_{i=1}^P Z(Y_i(t))^T + Z(Y_i(t)) \right) \right), \quad (7)$$

where M extracts and vectorizes the diagonal and upper triangle of a symmetric matrix, Z is the Fisher z -transformation (Zar, 2010):

$$Z(r) = \frac{\log(1+r) - \log(1-r)}{2} \quad (8)$$

R is the inverse of Z :

$$R(z) = \frac{\exp(2z-1)}{\exp(2z+1)}, \quad (9)$$

and $\mathbf{Y}_i(t)$ denotes the correlation matrix (Eqn. 2) between each column of \mathbf{X}_i and each column of the average observations from all *other* participants, $\bar{\mathbf{X}}_{\setminus i}$:

$$\bar{\mathbf{X}}_{\setminus i} = R \left(\frac{1}{P-1} \sum_{i \in \setminus i} Z(\mathbf{X}_i) \right), \quad (10)$$

62 where $\setminus i$ denotes the set of all participants other than participant i . In this way, the T by $\left(\frac{F^2-F}{2} + F\right)$ matrix $\bar{\mathbf{C}}$
63 is the time-varying extension of the ISFC approach developed by Simony et al. (2016).

64 Higher-order correlations

65 Given a timeseries of dynamic correlations (e.g., obtained using Eqn. 5), higher-order correlations reflect the
66 dynamic correlations between columns of \mathbf{Y} . Given unlimited computing resources, one could use repeated
67 applications of Equation 5 to estimate these higher-order correlations (i.e., substituting in the previous
68 output, \mathbf{Y} , for the input, \mathbf{X} in the equation). However, because each output \mathbf{Y} has $O(F^2)$ columns relative
69 to F columns in the input \mathbf{X} , the output of Equation 5 grows with the square of the number of repeated
70 applications (total cost of computing n^{th} order correlations is $O(F^{2n})$ for $n \in \mathcal{J}, n > 0$). When F or n is large,
71 this approach quickly becomes intractable.

72 To make progress in computing \mathbf{Y}_{n+1} , we can approximate \mathbf{Y}_n by computing an $O(F)$ -dimensional em-
73 bedding of \mathbf{Y}_n , termed $\hat{\mathbf{Y}}_n$, and then we can apply Equation 5 to $\hat{\mathbf{Y}}_n$ rather than directly to \mathbf{Y}_n . This enables
74 us to maintain $O(n)$ scaling with respect to n , rather than exponential scaling via the direct approach.

75 There are many possible methods for computing $\hat{\mathbf{Y}}_n$ from \mathbf{Y}_n , including traditional dimensionality
76 reduction approaches and graph theory based approaches as described next. In the *Discussion* section we
77 elaborate on other potential approaches.

78 Dimensionality reduction-based approaches to computing $\hat{\mathbf{Y}}_n$

79 Commonly used dimensionality reduction algorithms include Principal Components Analysis (PCA; Pear-
80 son, 1901), Probabilistic PCA (PPCA; Tipping & Bishop, 1999), Exploratory Factor Analysis (EFA; Spearman,
81 1904), Independent Components Analysis (ICA; Jutten & Herault, 1991; Comon et al., 1991), t -Stochastic
82 Neighbor Embedding (t -SNE; van der Maaten & Hinton, 2008), Uniform Manifold Approximation and
83 Projection (UMAP; McInnes & Healy, 2018), non-negative matrix factorization (NMF; Lee & Seung,
84 1999), Topographic Factor Analysis (TFA) Manning et al. (2014), Hierarchical Topographic Factor analysis
85 (HTFA) Manning et al. (2018), Topographic Latent Source Analysis (TLSA) Gershman et al. (2011), Dictio-
86 nary learning (J. B. Mairal et al., 2009; J. Mairal et al., 2009), deep autoencoders (Hinton & Salakhutdinov,

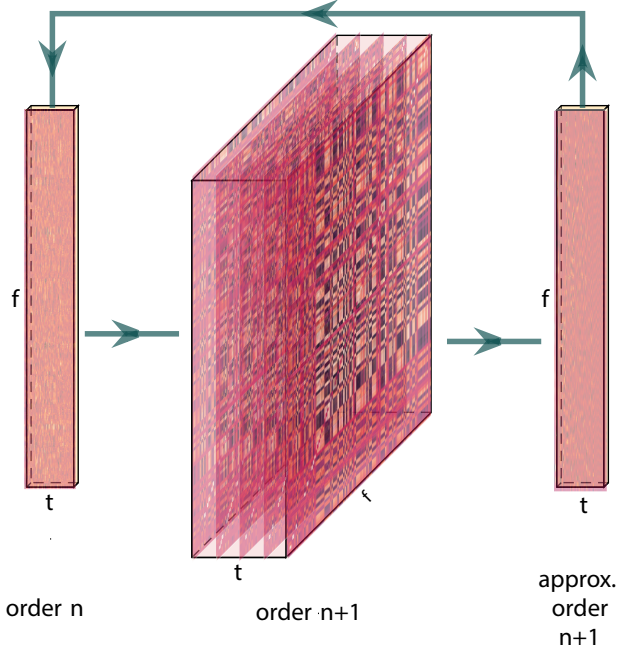


Figure 2: Computing higher order correlations. Dynamic correlations are computed then approximated to the same size as original data using dimensionality reduction. This process is repeated, and can be used to compute up to any arbitrary order with computations scaling linearly (as opposed to exponentially) with order.

87 2006), among others. While complete characterizations of each of these algorithms is beyond the scope of
 88 the present manuscript, the general intuition driving these approaches is to compute the $\hat{\mathbf{Y}}$ with i columns
 89 that is closest to the original \mathbf{Y} with j columns, and where (typically) $i \ll j$. The different approaches place
 90 different constraints on what properties $\hat{\mathbf{Y}}$ must satisfy and which aspects of the data are compared (and
 91 how) to characterize the match between $\hat{\mathbf{Y}}$ and \mathbf{Y} .

92 Applying dimensionality reduction algorithms to \mathbf{Y} yields a $\hat{\mathbf{Y}}$ whose columns reflect weighted combi-
 93 nations (or nonlinear transformations) of the original columns of \mathbf{Y} . This has two main consequences. First,
 94 with each repeated dimensionality reduction, the resulting $\hat{\mathbf{Y}}_n$ has lower and lower fidelity (with respect to
 95 what the “true” \mathbf{Y}_n might have looked like without using dimensionality reduction to maintain scalability).
 96 In other words, computing $\hat{\mathbf{Y}}_n$ is a lossy operation. Second, whereas the columns of \mathbf{Y}_n may be mapped
 97 directly onto pairs of columns of \mathbf{Y}_{n-1} , that mapping either becomes less cleanly defined in $\hat{\mathbf{Y}}_n$ due to the
 98 reweightings and/or nonlinear transformations.

99 **Graph theory-based approaches to computing $\hat{\mathbf{Y}}_n$**

100 Graph theoretic measures take as input a matrix of interactions (e.g., using the above notation, an $F \times F$
 101 correlation matrix or binarized correlation matrix reconstituted from a single timepoint’s row of \mathbf{Y}) and

102 return as output a set of F measures describing how each node (feature) sits within that interactions matrix
103 with respect to the rest of the population. Common measures include betweenness centrality (the proportion
104 of shortest paths between each pair of nodes in the population that involves the given node in question; e.g.,
105 Newman, 2005; Opsahl et al., 2010; Barthélemy, 2004; Geisberger et al., 2008; Freeman, 1977); diversity and
106 dissimilarity (characterizations of how differently connected a given node is from others in the population;
107 e.g., Rao, 1982; Lin, 2009; Ricotta & Szeidl, 2006); Eigenvector centrality and pagerank centrality (measures of
108 how influential a given node is within the broader network; e.g., Newman, 2008; Bonacich, 2007; Lohmann
109 et al., 2010; Halu et al., 2013); transfer entropy and flow coefficients (a measure of how much information is
110 flowing from a given node to other nodes in the network; e.g., Honey et al., 2007; Schreiber, 2000); k -coreness
111 centrality (a measure of the connectivity of a node within its local sub-graph; e.g., Alvarez-Hamelin et al.,
112 2005; Christakis & Fowler, 2010); within-module degree (a measure of how many connections a node has to
113 its close neighbors in the network; e.g., Rubinov & Sporns, 2010); participation coefficient (a measure of the
114 diversity of a node's connections to different sub-graphs in the network; e.g., Rubinov & Sporns, 2010); and
115 sub-graph centrality (a measure of a node's participation in all of the network's sub-graphs; e.g., Estrada &
116 Rodríguez-Velázquez, 2005).

117 As an alternative to the above dimensionality reduction approach to embedding \mathbf{Y}_n in a lower-dimensional
118 space, but still allowing for scalable explorations of higher-order structure in the data, we also explore using
119 the above graph theoretic measures as a means of obtaining $\hat{\mathbf{Y}}_n$. In particular: for a given graph theoretic
120 measure, $\eta : \mathcal{R}^{F \times F} \rightarrow \mathcal{R}^F$, we can use η to transform each row of \mathbf{Y}_n in a way that characterizes the cor-
121 responding graph-theoretic properties of each column. Whereas the dimensionality reduction approach
122 to computing $\hat{\mathbf{Y}}_n$ is lossy, the graph-theory approach is lossless. However, whereas the dimensionality
123 reduction approach maintains ties (direct or indirect) to the original activity patterns reflected in \mathbf{Y}_{n-1} , the
124 graph-theory approach does not. Instead, the graph-theory characterizes the nature and timecourse of each
125 feature's *participation* in the network.

126 Evaluation metrics

127 We evaluate our approach to extracting dynamic correlations and higher-order correlations using several
128 metrics detailed next. First, we generated synthetic data using known time-varying correlations, and then
129 we evaluated the fidelity with which Equation 5 could recover those correlations (for synthetic datasets
130 with different properties, and using different kernels to define the weights; Fig. 1). We then turned to a
131 series of analyses on a (real) neuroimaging dataset where the ground truth correlations were *not* known.
132 We evaluated whether the recovered correlations could be used to accurately label held-out neuroimaging

133 data with the time at which it was collected. We used this latter evaluations (using timepoint decoding)
134 as a proxy for gauging how much explanatory power the recovered correlations held with respect to the
135 observed data.

136 **Generating synthetic data**

137 To explore recovery of a constant covariance (Fig. 3, a.), we generated synthetic data sampled from a constant
138 covariance matrix. To do this, we created one random covariance matrix, K , with 50 features, and for each
139 of the 300 timepoints we sampled from a Gaussian distribution centered on K . Similarly, we generated
140 synthetic data sampled from a random covariance matrix (Fig. 3, b.) by creating a new random covariance
141 matrix $K(t)$, for each of the 300 timepoints and sampled from a Gaussian distribution centered on $K(t)$.

To generate synthetic data from a dynamically changing covariance matrix (Fig. 3, c.), we generated two
random covariance matrices, K_1 and K_2 . We then computed a weighted average covariance matrix for each
of the 300 timepoint, $K(t)$, by taking the linearly spaced weights (w) of the two random matrices,

$$K(t) = w(t) * K_1 + (1 - w(t)) * K_2, \quad (11)$$

$$(12)$$

142 and for each of the 300 timepoints sampled from a Gaussian distribution centered on $K(t)$.

143 Lastly, for the synthetic data containing block structure (Fig. 3, d.), we followed the same process of
144 creating synthetic data sampled from a constant covariance matrix (see above) but sampled from a new
145 random covariance matrix after 60 consecutive timepoints. We then pieced the blocks together to create a
146 synthetic dataset with 300 total timepoints but drawn from 5 separate covariance matrices.

147 **Recovery of ground truth parameters from synthetic data**

148 We applied timecorr, using delta and gaussian (width = 10) kernels Fig. 1 to each of these synthetic datasets,
149 then correlated each recovered correlation matrix with the ground truth. We repeated this process 10 times
150 and explored how recovery varies with the kernel and the specific structure of the data. For the ramping
151 synthetic dataset (Fig. 3, c.) and for the block synthetic dataset (Fig. 3, d.) we made further comparisons
152 of the timecorr recovered correlation matrices. We compared the ramping recovered correlation matrices to
153 only the first random covariance matrix K_1 (First, Fig. 3, c.) and to only the last random covariance matrix
154 K_2 (Last, Fig. 3, c.) from Equation 12. We also compared the block recovered correlation matrices in to the
155 block specific covariance matrix (Block 1-5, Fig. 3, d.).

156 **Timepoint decoding**

157 To explore how higher-order structure varies with stimulus structure and complexity, we used a previous
158 neuroimaging dataset Simony et al. (2016) in which participants listened to an audio recording of a story;
159 36 participants listen to an intact version of the story, 17 participants listen to time-scrambled recordings of
160 the same story where paragraphs were scrambled, 36 participants listen to word-scrambled version and 36
161 participants lay in rest condition.

162 Prior work has shown participants share similar neural responses to richly structured stimuli when
163 compared to stimuli with less structure. To assess whether the moment-by-moment higher order correlations
164 were reliably preserved across participants, we used inter-subject functional connectivity (ISFC) to isolate
165 the time-varying correlational structure (functional connectivity patterns that were specifically driven by
166 the story participants listened to. Following the analyses conducted by (HTFA) Manning et al. (2018), we
167 first applied *hierarchical topographic factor analysis* (HTFA) to the fMRI datasets to obtain a time series of
168 700 node activities for every participant. We then computed the dynamic weighted ISFC using a range of
169 kernels and widths. Specifically, we used Gaussian, Laplace, and mexican hat kernels, as well as widths of
170 5, 10, 20, and 50. We then approximated these dynamic correlation using two reduction measures, PCA and
171 eigenvector centrality, and computed the dynamic weighted ISFC on the approximations. We repeated this
172 process up to 10th order approximated correlations.

173 To assess decoding accuracy, we randomly divided participants for each stimulus into training and
174 testing groups. For the zeroth order, we computed the mean factor activity for each group. For all subsequent
175 orders up to the tenth order, we computed the mean approximated dynamic ISFC of factor activity for each
176 group. To assess how additional higher-order correlations contribute to decoding accuracy, for each order
177 we included a weighted-mixture (described below) of the activity patterns of all previous orders. For each
178 group of participants in turn, we compared these activity patterns (using Pearson correlations) to estimate
179 the story times each pattern corresponded to. Specifically, we asked, for each timepoint: what are the
180 correlations between the first group's and second group's activity patterns at each order. We note that the
181 decoding test we used is a conservative in which we count a timepoint label as incorrect if it is not an exact
182 match.

183 For each order we obtained the weighted-mixture of the correlation matrices for the current order and
184 all previous orders using mixing parameter, ϕ , where $0 < \phi < 1$ reflects a weighted mixture of order based
185 decoding Fig. 4 Panel c.). We calculated ϕ , by subdividing the training group and using the quasi-Newton
186 method of Broyden, Fletcher, Goldfarb, and Shanno (BFGS (Nocedal & Wright, 2006)) for optimization. We
187 repeated this cross-validation process 10 times for each parameter set.

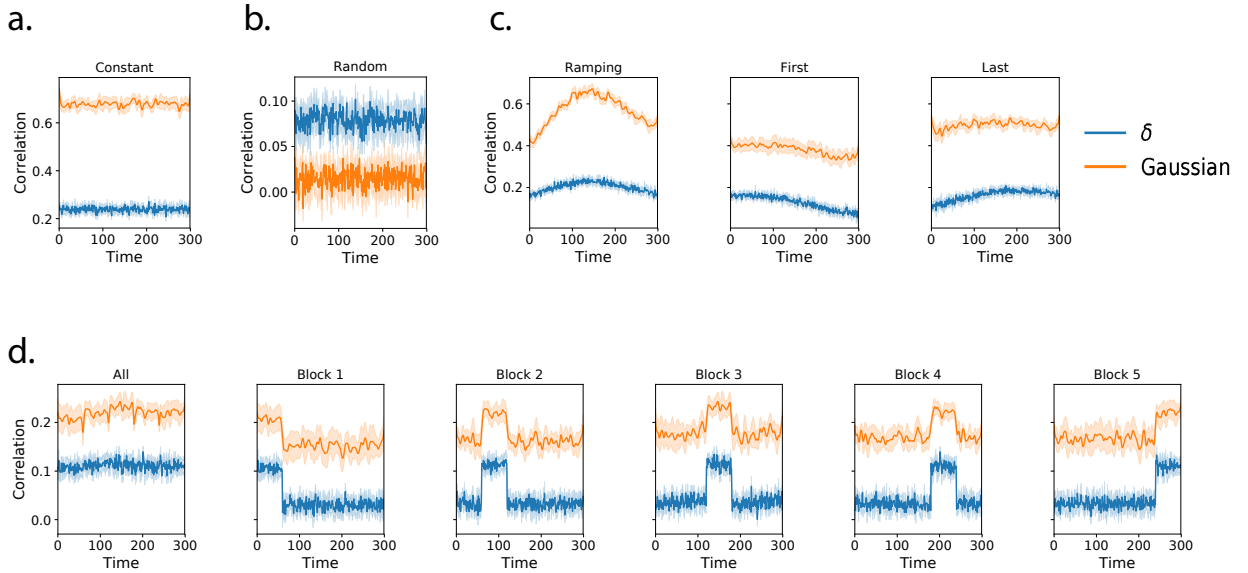


Figure 3: Dynamic correlation recovery with synthetic data. Using synthetic data containing different underlying correlational structure, we test how well we can recover dynamic correlation matrices using two kernels (delta and gaussian, width = 10) when compared to ground truth. We plot recovery using of datasets containing the following underlying structure: **a. Constant.** **b. Random.** **c. Ramping.** **d. Block.**

188 Results

189 Synthetic data

190 To assess the performance of dynamic correlation recovery using `timecorr`, we varied width the kernel and
 191 the specific structure of the data. We applied `timecorr`, using delta and gaussian kernels Fig. 1) to each of
 192 the following synthetic datasets: constant, random, ramping, and block. We then correlated each recovered
 193 correlation matrix with the ground truth.

194 For the constant synthetic dataset, a gaussian kernel (width=10) outperformed the delta kernel (Fig. 3,
 195 a.). This is in contrast with the random synthetic dataset, for which the delta kernel best captures the rapidly
 196 changing structure (Fig. 3, b.). For the ramping synthetic dataset, the slow changing strucutre within the
 197 data is best captured by the gaussian kernel and the best recovery occurs in the middle (Ramping, Fig. 3,
 198 c.). In addition to comparing the `timecorr` recovered correlation matrices to the ground truth, we further
 199 compared the ramping recovered correlation matrices to only the first random covariance matrix K_1 (First,
 200 Fig. 3, c.) and to only the last random covariance matrix K_2 (Last, Fig. 3, c.), both of which perform best at
 201 the beginning and end respectively.

202 Similary for the block sythetic dataset, we compared the `timecorr` recovered correlation matrices to
 203 the ground truth as well as to each block-specific covariance matrix (Block 1-5, Fig. 3, d.). Although the

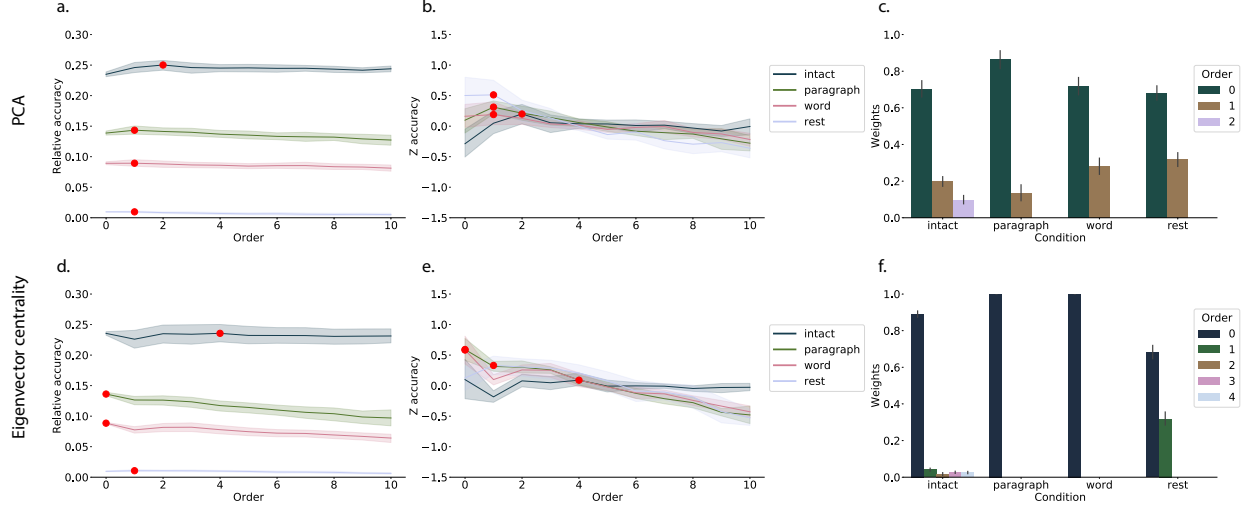


Figure 4: Decoding by order. **a.&d.** **Relative decoding accuracy by order.** Ribbons of each color display cross-validated decoding performance averaged over all parameters for each condition (intact, paragraph, word, and rest) using PCA (a.) or eigenvector centrality (d.) to approximate correlations. Decoders were trained using increasingly more higher-order information and this ribbons are displayed relative to chance at 0. The red dots indicates maximum decoding accuracy for each condition. **b.&e.** **Z-transformed decoding accuracy by order.** We Z-transformed the decoding accuracy by order to better visualize the order with the maximum decoding accuracy for each condition using PCA (b.) or eigenvector centrality (e.) to approximate correlations. **c.&f.** **Optimized weights.** Bar heights indicate the optimized mixing parameter ϕ of each contributing order up to and including the order with the maximum decoding accuracy for each contributing order using PCA (c.) or eigenvector centrality (f.) to approximate correlations. For the order with maximum decoding accuracy by condition, we show barplots of the optimized weights ϕ for each contributing order.

204 structure is changing by block, the gaussian kernel once again outperforms the delta kernel. Performance
 205 does however drop near even boundaries for when using the gaussian kernel.

206 Neuroimaging dataset (Simony et al., 2016)

207 For our decoding analysis, we used HTFA-derived node activities Manning et al. (2018) from fMRI data
 208 collected as participants listened to an audio recording of a story (intact condition; 36 participants), lis-
 209 tened to time scrambled recordings of the same story (17 participants in the paragraph-scrambled condition
 210 listened to the paragraphs in a randomized order and 36 in the word-scrambled condition listened to
 211 the words in a randomized order), or lay resting with their eyes open in the scanner (rest condition; 36
 212 participants). We sought to demonstrate how higher-order correlations may be used to examine dynamic
 213 interactions of brain patterns in (real) multi-subject fMRI datasets. This story listening dataset was col-
 214 lected as part of a separate study, where the full imaging parameters, image preprocessing methods, and
 215 experimental details may be found (Simony et al., 2016). The dataset is available at [http://arks.prince-
 216 ton.edu/ark:/88435/dsp015d86p269k](http://arks.princeton.edu/ark:/88435/dsp015d86p269k).

217 We next evaluated if our model of high-order correlations in brain activity can capture cognitively
218 relevant brain patterns. We performed a decoding analysis, using cross validation to estimate (using other
219 participants' data) which parts of the story each weighted-mixture of higher-order brain activity pattern
220 corresponded to (see *Materials and methods*). We note that our primary goal was not to achieve perfect
221 decoding accuracy, but rather to use decoding accuracy as a benchmark for assessing whether different
222 neural features specifically capture cognitively relevant brain patterns.

223 Separately for each experimental condition, we divided participants into two groups. For the zeroth
224 order, we computed the mean factor activity for each group. For all subsequent orders up to the tenth
225 order, we computed the mean approximated dynamic ISFC of factor activity for each group (see *Materials*
226 and *methods*), and combined in a weighted mixutre with all previous orders (i.e. cross-validation for the
227 second order contained a weighted-mixture of zeroth, first, and second order (Fig. 4, c.&f.). For each
228 order, we correlated the group 1 activity patterns with group 2 activity patterns. We then subdivided
229 the group 1 to obtain an optimal weighting parameter for each order's correlation matrix using the same
230 cross validation method. We used the optimal weighting parameters to obtain a weighted-mixture (see
231 *Materials and methods*) of each order's correlation matrix. Using these correlations, we labeled the group 1
232 timepoints using the group 2 timepoints with which they were most highly correlated; we then computed
233 the proportion of correctly labeled group 1 timepoints. (We also performed the symmetric analysis whereby
234 we labeled the group 2 timepoints using the group 1 timepoints as a template.) We repeated this procedure
235 100 times (randomly re-assigning participants to the two groups each time) to obtain a distribution of
236 decoding accuracies for each experimental condition. There were 272 timepoints for paragraph condition,
237 300 timepoints for intact and word conditions, and 400 timepoints for rest condition, so chance performance
238 on this decoding test is was $\frac{1}{272}$, $\frac{1}{300}$, and $\frac{1}{400}$ respectively.

239 We repeated this process for each set of parameters, varying kernel type and width, and averaged over the
240 reduction technique used to approximate the higher-order correlations (PCA Fig. 4, a.-c. and eigenvector
241 centrality Fig. 4, d.-f.). Since there is no ground truth in these analyses, and we did not know which
242 parameters best capture the data, we instead report a robustness search by averaging over the parameters
243 and reporting which results consistently showed up across all parameters.

244 The two methods used to approximate the higher-order correlations (PCA Fig. 4, a.-c. and eigenvector
245 centrality Fig. 4, d.-f.) capture different facets of the activity patterns. Using PCA, the higher-order
246 correlations are all linked to the original activity patterns, whereas eigenvectory centrality breaks the
247 immediate link with specific brain areas and instead characterizes the position of the nodes in the network
248 that are similar over time.

249 We found for both PCA and eigenvector centrality, during the intact condition in the experiment,

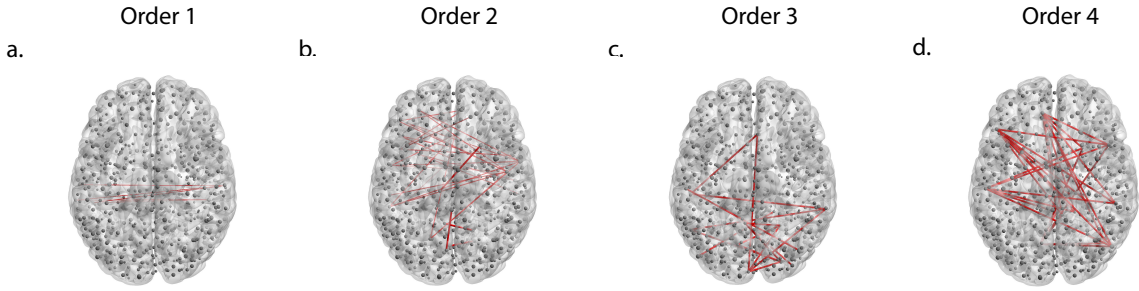


Figure 5: Average correlations by order for the intact listening condition. Using eigenvector centrality to approximate higher-order correlations for the intact listening condition, we plot the strongest 25% absolute value mean correlation for order: **a. 1. b. 2. c. 3., and d. 4.**, representing the degree of agreement by location pair over time.

250 classifiers that incorporated higher-order correlations yielded consistently higher accuracy than classifiers
 251 trained only on lower-order patterns (Fig. 4, a.&d.). We plot the average correlations for up to the fourth
 252 order for the intact condition (Fig. 5) representing the degree of agreement by location pair over time. By
 253 contrast, we found that incorporating higher-order (greater than first order) correlations did not further
 254 improve decoding accuracy for the other listening conditions or rest condition. This suggests that the
 255 cognitive processing that supported the most cognitively rich condition involved higher-order network
 256 dynamics.

257 Discussion

258 Based on prior work (?) and following the direction of the field (Turk-Browne, 2013) we think our thoughts
 259 might be encoded in dynamic network patterns, and possibly higher order network patterns (Fig. 6). We
 260 sought to test this hypothesis by developing an approach to inferring high-order network dynamics from
 261 timeseries data.

262 One challenge in studying dynamic interactions is the computational resources required to calculate
 263 higher-order correlations. We developed a computationally tractable model of network dynamics (Fig. 2)
 264 that takes in a feature timeseries and outputs approximated first-order dynamics (i.e., dynamic functional
 265 correlations), second-order dynamics (reflecting homologous networks that dynamically form and disperse),
 266 and higher-order network dynamics (up to tenth-order dynamic correlations).

267 We first validated our model using synthetic data, and explored how recovery varied with different
 268 underlying data structures and kernels. We then applied the approach to an fMRI dataset (Simony et al.,
 269 2016) in which participants listened to an audio recording of a story, as well as scrambled versions of the

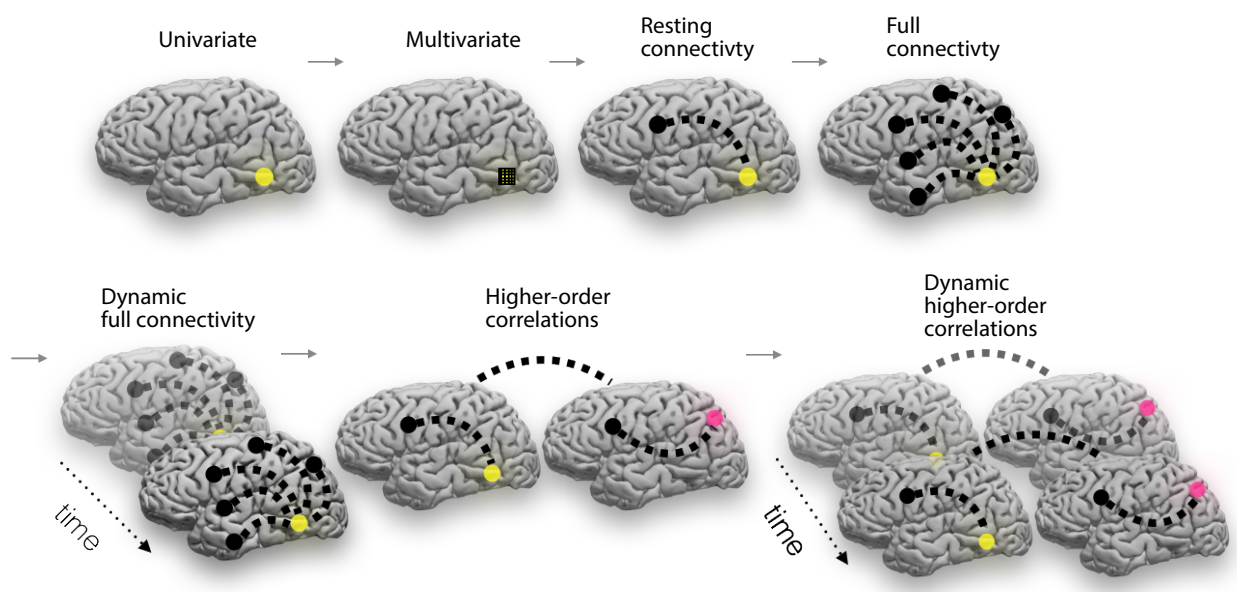


Figure 6: Direction of the field (adapted from (Turk-Browne, 2013)). The evolution of fMRI analyses started with univariate activation, which refers to the average amplitude of BOLD activity evoked by events of an experimental condition. Next, multivariate classifiers are trained on patterns of activation across voxels to decode distributed representations for specific events. The next, resting connectivity, is the temporal correlation of one or more seed regions with the remainder of the brain during rest. Additionally, task-based connectivity examines how these correlations differ by cognitive state. Following this increasing trajectory of increasing complexity, full connectivity considers all pairwise correlations in the brain, most commonly at rest. Next, dynamic full connectivity considers how full connectivity changes over time. Continuing this line of reasoning, we expect higher-order network dynamics might provide even richer insights into the neural basis of cognition.

270 same story (where the scrambling was applied at different temporal scales). We trained classifiers to take
271 the output of the model and decode the timepoint in the story (or scrambled story) that the participants
272 were listening to. We found that, during the intact listening condition in the experiment, classifiers that
273 incorporated higher-order correlations yielded consistently higher accuracy than classifiers trained only
274 on lower-order patterns (Fig. 4, a.&d.). By contrast, these higher-order correlations were not necessary
275 to support decoding the other listening conditions and (minimally above chance) during a control rest
276 condition. This suggests that the cognitive processing that supported the most cognitively rich listening
277 conditions involved second-order (or higher) network dynamics.

278 Although we found decoding accuracy was best when incorporating higher-order network dynamics
279 for all but rest condition, it is unclear if this is a product of the brain or the data collection technique. It could
280 be that the brain is second-order or it could be that fMRI can only reliably give second-order interactions.
281 Exploring this method with other data collection technique will be important to disentangle this question.

282 **Concluding remarks**

283 How can we better understand how brain patterns change over time? How can we quantify the potential
284 network dynamics that might be driving these changes? One way to judge the techniques of the future is
285 to look at the trajectory of the fMRI field so far has taken so far (Fig. 2). The field started with univariate
286 activation, measuring the average activity for each voxel. Analyses of multivariate activation followed,
287 looking at spatial patterns of activity over voxels. Next, correlations of activity were explored, first with
288 measures like resting connectivity that take temporal correlation between a seed voxel and all other voxels
289 then with full connectivity that measure all pairwise correlations. Additionally, this path of increasing
290 complexity also moved from static to dynamic measurements. One logical next step in this trajectory would
291 be dynamic higher-order correlations. We have created a method to support these calculations by scalably
292 approximating dynamic higher-order correlations.

293 **Acknowledgements**

294 We acknowledge discussions with Luke Chang, Hany Farid, Paxton Fitzpatrick, Andrew Heusser, Eshin
295 Jolly, Qiang Liu, Matthijs van der Meer, Judith Mildner, Gina Notaro, Stephen Satterthwaite, Emily Whitaker,
296 Weizhen Xie, and Kirsten Ziman. Our work was supported in part by NSF EPSCoR Award Number 1632738
297 to J.R.M. and by a sub-award of DARPA RAM Cooperative Agreement N66001-14-2-4-032 to J.R.M. The
298 content is solely the responsibility of the authors and does not necessarily represent the official views of our

299 supporting organizations.

300 Author contributions

301 Concept: J.R.M. Implementation: T.H.C., L.L.W.O., and J.R.M. Analyses: L.L.W.O and J.R.M.

302 References

- 303 Alvarez-Hamelin, I., Dall'Asta, L., Barrat, A., & Vespignani, A. (2005). *k*-corr decomposition: a tool for the
304 visualization of large scale networks. *arXiv*, cs/0504107v2.
- 305 Barthélemy, M. (2004). Betweenness centrality in large complex networks. *European Physical Journal B*, 38,
306 163–168.
- 307 Bonacich, P. (2007). Some unique properties of eigenvector centrality. *Social Networks*, 29(4), 555–564.
- 308 Chang, C., & Glover, G. H. (2010). Time-frequency dynamics of resting-state brain connectivity measured
309 with fMRI. *NeuroImage*, 50, 81–98.
- 310 Christakis, N. A., & Fowler, J. H. (2010). Social network sensors for early detection of contagious outbreaks.
311 *PLoS One*, 5(9), e12948.
- 312 Comon, P., Jutten, C., & Herault, J. (1991). Blind separation of sources, part II: Problems statement. *Signal
313 Processing*, 24(1), 11 - 20.
- 314 Demertzi, A., Tagliazucchi, E., Dehaene, S., Deco, G., Barttfeld, P., Raimondo, F., . . . Sitt, J. D. (2019). Human
315 consciousness is supported by dynamic complex patterns of brain signal coordination. *Science Advances*,
316 5(2), eaat7603.
- 317 Estrada, E., & Rodríguez-Velázquez, J. A. (2005). Subgraph centrality in complex networks. *Physical Review
318 E*, 71(5), 056103.
- 319 Freeman, L. C. (1977). A set of measures of centrality based on betweenness. *Sociometry*, 40(1), 35–41.
- 320 Geisberger, R., Sanders, P., & Schultes, D. (2008). Better approximation of betweenness centrality. *Proceedings
321 of the meeting on Algorithm Engineering and Experiments*, 90–100.
- 322 Gershman, S., Blei, D., Pereira, F., & Norman, K. (2011). A topographic latent source model for fMRI data.
323 *NeuroImage*, 57, 89–100.

- 324 Halu, A., Mondragón, R. J., Panzarasa, P., & Bianconi, G. (2013). Multiplex PageRank. *PLoS One*, 8(10),
325 e78293.
- 326 Hinton, G. E., & Salakhutdinov, R. R. (2006). Reducing the dimensionality of data with neural networks.
327 *Science*, 313(5786), 504–507.
- 328 Honey, C. J., Kötter, R., Breakspear, M., & Sporns, O. (2007). Network structure of cerebral cortex shapes
329 functional connectivity on multiple time scales. *Proceedings of the National Academy of Science USA*, 104(24),
330 10240–10245.
- 331 Jutten, C., & Herault, J. (1991). Blind separation of sources, part I: An adaptive algorithm based on
332 neuromimetic architecture. *Signal Processing*, 24(1), 1–10.
- 333 Lee, D. D., & Seung, H. S. (1999). Learning the parts of objects by non-negative matrix factorization. *Nature*,
334 401, 788–791.
- 335 Lin, J. (2009). Divergence measures based on the Shannon entropy. *IEEE Transactions on Information Theory*,
336 55(1), 145–151.
- 337 Lohmann, G., Margulies, D. S., Horstmann, A., Pleger, B., Lepsius, J., Goldhahn, D., ... Turner, R. (2010).
338 Eigenvector centrality mapping for analyzing connectivity patterns in fMRI data of the human brain.
339 *PLoS One*, 5(4), e10232.
- 340 Mairal, J., Ponce, J., Sapiro, G., Zisserman, A., & Bach, F. R. (2009). Supervised dictionary learning. *Advances
341 in Neural Information Processing Systems*, 1033–1040.
- 342 Mairal, J. B., Bach, F., Ponce, J., & Sapiro, G. (2009). Online dictionary learning for sparse coding. *Proceedings
343 of the 26th annual international conference on machine learning*, 689–696.
- 344 Manning, J. R., Ranganath, R., Norman, K. A., & Blei, D. M. (2014). Topographic factor analysis: a Bayesian
345 model for inferring brain networks from neural data. *PLoS One*, 9(5), e94914.
- 346 Manning, J. R., Zhu, X., Willke, T. L., Ranganath, R., Stachenfeld, K., Hasson, U., ... Norman, K. A. (2018).
347 A probabilistic approach to discovering dynamic full-brain functional connectivity patterns. *NeuroImage*,
348 180, 243–252.
- 349 McInnes, L., & Healy, J. (2018). UMAP: Uniform manifold approximation and projection for dimension
350 reduction. *arXiv*, 1802(03426).
- 351 Newman, M. E. J. (2005). A measure of betweenness centrality based on random walks. *Social Networks*, 27,
352 39–54.

- 353 Newman, M. E. J. (2008). The mathematics of networks. *The New Palgrave Encyclopedia of Economics*, 2, 1–12.
- 354 Nocedal, J., & Wright, S. J. (2006). *Numerical optimization*. New York: Springer.
- 355 Opsahl, T., Agneessens, F., & Skvoretz, J. (2010). Node centrality in weighted networks: generalizing degree
356 and shortest paths. *Social Networks*, 32, 245–251.
- 357 Pearson, K. (1901). On lines and planes of closest fit to systems of points in space. *The London, Edinburgh,
358 and Dublin Philosophical Magazine and Journal of Science*, 2, 559–572.
- 359 Rao, C. R. (1982). Diversity and dissimilarity coefficients: a unified approach. *Theoretical Population Biology*,
360 21(1), 24–43.
- 361 Ricotta, C., & Szeidl, L. (2006). Towards a unifying approach to diversity measures: Bridging the gap
362 between the Shannon entropy and Rao's quadratic index. *Theoretical Population Biology*, 70(3), 237–243.
- 363 Rubinov, M., & Sporns, O. (2010). Complex network measures of brain connectivity: uses and interpreta-
364 tions. *NeuroImage*, 52, 1059–1069.
- 365 Schreiber, T. (2000). Measuring information transfer. *Physical Review Letters*, 85(2), 461–464.
- 366 Simony, E., Honey, C. J., Chen, J., & Hasson, U. (2016). Uncovering stimulus-locked network dynamics
367 during narrative comprehension. *Nature Communications*, 7(12141), 1–13.
- 368 Spearman, C. (1904). General intelligence, objectively determined and measured. *American Journal of
369 Psychology*, 15, 201–292.
- 370 Tipping, M. E., & Bishop, C. M. (1999). Probabilistic principal component analysis. *Journal of Royal Statistical
371 Society, Series B*, 61(3), 611–622.
- 372 Turk-Browne, N. B. (2013). Functional interactions as big data in the human brain. *Science*, 342, 580–584.
- 373 van der Maaten, L. J. P., & Hinton, G. E. (2008). Visualizing high-dimensional data using t-SNE. *Journal of
374 Machine Learning Research*, 9, 2579–2605.
- 375 Zar, J. H. (2010). *Biostatistical analysis*. Prentice-Hall/Pearson.